



HAL
open science

Stochastic representation of the Reynolds transport theorem: revisiting large-scale modeling

Souleymane Kadri Harouna, Etienne Mémin

► **To cite this version:**

Souleymane Kadri Harouna, Etienne Mémin. Stochastic representation of the Reynolds transport theorem: revisiting large-scale modeling. *Computers and Fluids*, 2017, 156, pp.456-469. 10.1016/j.compfluid.2017.08.017 . hal-01394780v2

HAL Id: hal-01394780

<https://inria.hal.science/hal-01394780v2>

Submitted on 15 Aug 2017

HAL is a multi-disciplinary open access archive for the deposit and dissemination of scientific research documents, whether they are published or not. The documents may come from teaching and research institutions in France or abroad, or from public or private research centers.

L'archive ouverte pluridisciplinaire **HAL**, est destinée au dépôt et à la diffusion de documents scientifiques de niveau recherche, publiés ou non, émanant des établissements d'enseignement et de recherche français ou étrangers, des laboratoires publics ou privés.

Stochastic representation of the Reynolds transport theorem: revisiting large-scale modeling

S. Kadri Harouna^a, E. Mémin^b,

^a*Laboratoire Mathématiques, Image et Applications (MIA), Université de La Rochelle,
Avenue Michel Crépeau 17042 La Rochelle, France*

^b*INRIA Rennes, Campus Universitaire de Beaulieu, 35042 Rennes cedex, France*

Abstract

We explore the potential of a formulation of the Navier-Stokes equations incorporating a random description of the small-scale velocity component. This model, established from a version of the Reynolds transport theorem adapted to a stochastic representation of the flow, gives rise to a large-scale description of the flow dynamics in which emerges an anisotropic subgrid tensor, reminiscent to the Reynolds stress tensor, together with a drift correction due to an inhomogeneous turbulence. The corresponding subgrid model, which depends on the small scales velocity variance, generalizes the Boussinesq eddy viscosity assumption. However, it is not anymore obtained from an analogy with molecular dissipation but ensues rigorously from the random modeling of the flow. This principle allows us to propose several subgrid models defined directly on the resolved flow component. We assess and compare numerically those models on a standard Green-Taylor vortex flow at Reynolds numbers $Re=1600$, $Re=3000$ and $Re=5000$. The numerical simulations, carried out with an accurate divergence-free scheme, outperform classical large-eddies formulations and provides a simple demonstration of the pertinence of the proposed large-scale modeling.

Keywords: Large-scale fluid flow dynamics, stochastic transport, Subgrid model, turbulence, Taylor-Green flow

1. Introduction

The large-scale modeling of fluid flow dynamics remains nowadays a major research issue in fluid mechanics or in geophysics despite an enormous research effort since the first investigations on the subject 150 years ago [6]. The research themes behind this topic cover fundamental issues such as turbulence modeling and the analysis of fully developed turbulent flows, but also more applicative research problems related to the definition of practical numerical methods for the

Email address: `etienne.memin@inria.fr` (E. Mémin)

simulation of complex flows. In this latter case the difficulty consists in setting up a reliable modeling of the large-scale dynamics in which the contribution of unresolved small-scale processes are explicitly taken into account. For the Navier-Stokes equations, the problem is all the more difficult that the spatial and temporal scales are tightly interacting together.

The neglected processes include, among others things, the action of the unresolved motion scales, complex partially-known forcing, an incomplete knowledge of the boundary conditions and eventual numerical artifacts. Such unresolved processes must be properly taken into account to describe accurately the energy transfers and to construct stable numerical simulations. In real world situations, the complexity of the involved phenomenon prevents the use of an accurate – but inescapably expensive – deterministic modeling. We advocate instead the use of a stochastic modeling.

Within this prospect, we aim at describing the missing contributions through random fields encoding a flow component only in a probability distribution sense. Those variables correspond to the discrepancies or errors between the dynamical model and the actual dynamics. Their modeling is of the utmost importance in geophysics, either for data assimilation or forecasting issues. In both cases, an accurate modeling of the flow errors dynamics enables to maintain an ensemble of flow configurations with a sufficient but also meaningful diversity.

Small-scale processes are responsible both for an energy dissipation but also for local backscattering of energy [59]. The introduction of random variables in the flow dynamics has been considered by several authors, as it constitutes an appealing mechanism for the phenomenological modeling of intermittent processes associated to the inverse energy cascade [42, 48, 69]. Recently those models have regained a great interest for the modeling of geophysical flows [11, 28, 46, 47, 71] in climate sciences (see also the thematic issue [56] or the review [20]).

Numerous turbulence models proposed in the context of Large Eddies Simulations (LES) and Reynolds Average Simulations (RANS) introduce *de facto* an eddy viscosity assumption to model the energy dissipation due to unresolved scales [16, 43, 50, 72, 67]. This concept dates back to the work of Boussinesq [6] and Prandtl [62]. It relies on the hypothesis that the energy transfer from the resolved scales to the subgrid scales can be described in a similar way to the molecular viscosity mechanism. It is therefore not at all related to any uncertainty or error quantities. In models dealing explicitly with a statistical modeling of the turbulent fluctuations there is thus some incoherency in representing directly the dissipative mechanism attached to random terms through an eddy viscosity assumption. In this work we will not make use of such an hypothesis. Instead, we will rely on a general diffusion expression that emerges naturally from our formalism.

This subgrid model is properly derived from a general Lagrangian stochastic model of the fluid motion in which the fluid parcels displacement is decomposed in two components: a smooth differentiable (possibly random) function and a random field, uncorrelated in time but correlated in space. Such a decomposition consists in separating or "filtering" a rough velocity in a smooth slow time-scale component and a fast oscillating velocity field representing the unresolved

flow. Though there is, in general, no sharp time-scale separation in turbulent flows, the resolved velocity can be interpreted as a temporally coarse-grained component whereas the time-uncorrelated component stands for the small time-scale unresolved velocity. As a temporal smoothing imposes implicitly a spacial smoothing, this separation can be thus interpreted in terms of a LES filtering technique. Yet, the corresponding Eulerian formulation does not ensue from a filtering procedure. It is thus not prone to errors associated to the violation of the commutation assumption between the filter and the spatial derivatives [25, 24]. Besides, those equations introduce an effective advection related to the small-scale velocity inhomogeneity. This modified advection, empirically introduced in Langevin models of particle dispersion [45], corresponds exactly to a phenomenon, termed *turbophoresis*, related to the migration of inertial particles in regions of lower turbulent diffusivity [70].

The large-scale representation of the Navier-Stokes equations on which we rely in this study are built from a stochastic version of the Reynolds transport theorem [49]. This modified Reynolds transport theorem, which constitutes here the cornerstone of our large-scale dynamics representation, is presented in the following section. General invariance properties of the corresponding large-scale dynamics such as scale and Galilean invariances are detailed in a comprehensive appendix. In section 3 several novel subgrid tensors will be devised and compared on a standard Green-Taylor vortex flow [74]. We will show that all the proposed schemes outperform the usual dynamic Smagorinsky subgrid formulation [22, 23, 44, 72].

2. Stochastic modeling of fluid flow dynamics

Numerous methodological choices can be envisaged to devise stochastic representations of the Navier-Stokes equations. The simplest method considers additional random forcing to the dynamics. This is the choice that has been the most often performed since the work of Benssoussan [3]. Another choice, in the wake of Kraichnan’s work [35], consists in closing the large-scale flow representation in the Fourier space by relying on a Langevin equation [37, 31, 41]. Obviously the frontiers between those two methodologies are sometimes fuzzy, and numerous works rely on both strategies in order to devise the shape that should take the random variables evolution law [31, 69]. Lagrangian stochastic models based on Langevin equations have been also intensively used for turbulent dispersion [68] or in probability density function (PDF) modeling of turbulent flows [29, 61]. Those Lagrangian models, which require to model the drift and diffusion functions, lead to very attractive particle based representations of complex flows [51, 60]. They are nevertheless not adapted to global large-scale Eulerian representations of the flow dynamics.

In this work, we will rely on a different framework in specifying the stochastic nature of the velocity from the very beginning as proposed in [30, 49]. The basic idea is built on the assumption that the Lagrangian fluid particles displacement results from a smooth velocity component and a highly oscillating stochastic

velocity component uncorrelated in time,

$$\mathbf{X}_t = \mathbf{X}_{t_0} + \int_{t_0}^t \mathbf{w}(\mathbf{X}_s, s) ds + \int_{t_0}^t \boldsymbol{\sigma}(\mathbf{X}_s, s) d\mathbf{B}_s, \quad (1)$$

with the velocity components:

$$\mathbf{U}(\mathbf{X}_t, t) = \mathbf{w}(\mathbf{X}_t, t) + \dot{\mathbf{W}}(\mathbf{X}_t, t). \quad (2)$$

In this decomposition the first right-hand term is a smooth function of time associated to the large-scale velocity component. The second term stands for the small-scale velocity field. It is a white noise velocity component defined from the (formal) time-derivative of the random field: $\dot{\mathbf{W}}(\mathbf{X}_t, t) = \boldsymbol{\sigma}(\mathbf{X}_t, t) \frac{d}{dt} \mathbf{B}_t$. This random field is a three-dimensional centered Wiener process; it is thus uncorrelated in time but can be anisotropic and inhomogeneous in space. Since we focus in this study only on incompressible flows, the small-scale component is defined as a divergence-free random field; it is hence associated to a divergence-free diffusion tensor:

$$\nabla \cdot \boldsymbol{\sigma} = 0. \quad (3)$$

Analogously to the standard deterministic case, the derivation procedure from the physical conservation laws of the Navier-Stokes equations is based primarily on the Reynolds transport theorem (RTT).

2.1. Stochastic Reynolds transport theorem

The RTT provides the expression of the rate of change of a scalar function, q , within a material volume, $\mathcal{V}(t)$. For a stochastic flow (2) with an incompressible small-scale velocity component ($\nabla \cdot \boldsymbol{\sigma} = 0$), this expression derived in [49, 64], is given by:

$$d \int_{\mathcal{V}(t)} q d\mathbf{x} = \int_{\mathcal{V}(t)} \left(d_t q + \left[\nabla \cdot \left(q \underbrace{\left(\mathbf{w} - \frac{1}{2} \nabla \cdot \mathbf{a} \right)}_{\tilde{\mathbf{w}}} \right) - \frac{1}{2} \sum_{i,j=1}^d \partial_{x_i} (a_{ij} \partial_{x_j} q) \right] dt + \nabla q \cdot \boldsymbol{\sigma} d\mathbf{B}_t \right) d\mathbf{x}. \quad (4)$$

This modified RTT involves the time increment of the random scalar quantity q (the differential of q at a fixed point) instead of the time derivative. A diffusion operator emerges also naturally. For clarity's sake, this term is designated as “subgrid stress tensor” following the protocols of large eddies simulation (LES). However, its construction is quite different. It is not based on Boussinesq's eddy viscosity assumption nor on any structural turbulence models [67] but arises directly from stochastic calculus rules. It expresses the mixing process exerted on the scalar quantity by the fast oscillating velocity component. This diffusion term is directly related to the small-scale component through the *variance tensor*, \mathbf{a} , defined from the diagonal of the small-scale velocity covariance:

$$\mathbf{a}(\mathbf{x}, t) \delta(t - t') dt = \mathbb{E} \left((\boldsymbol{\sigma}(\mathbf{x}, t) d\mathbf{B}_t) (\boldsymbol{\sigma}(\mathbf{x}, t') d\mathbf{B}_{t'})^T \right),$$

it can be checked that the variance tensor corresponds to an eddy viscosity term (with units in m^2s^{-1}). This term plays thus a role similar to the eddy viscosity models introduced in classical large scale representations [2, 21, 44, 72] or to the spectral vanishing viscosity [34, 57, 73]. It is also akin to numerical regularization models considered in implicit models [1, 5, 15, 39, 76, 78] (see also the textbook [26] for a recent and complete survey). Our approach is nevertheless more general as it does not rely on *a priori* fixed shape of the Reynolds stress (e.g. Boussinesq assumption) nor does it presuppose a given numerical discrete scheme (e.g. implicit models).

A corrective advection term, $\tilde{\mathbf{w}} = \mathbf{w} - 1/2\nabla \cdot \mathbf{a}$, appears also in the stochastic RTT formulation. This correction expresses the influence of the small scales inhomogeneity on the large ones. A drift is engendered from the regions associated with maximal variance (maximal turbulent kinetic energy - TKE) toward the area of minimum variance (e.g. minimal TKE). This corresponds to the *turbophoresis* phenomenon associated with turbulence inhomogeneity, which drives inertial particles toward the regions of lower diffusivity [9, 14, 70]. For homogeneous noise, the variance tensor is constant and this corrective advection does not come into play. It can be noted that this advection correction is of the same form as the one proposed in [45].

Through this modified RTT, stochastic versions of the mass and momentum conservation equations can be (almost) directly derived. Incompressibility conditions can for instance be immediately deduced from the RTT applied to $q = 1$ and the flow jacobian (J):

$$\int_{\mathcal{V}(t_0)} d(J(\mathbf{X}_t(\mathbf{x}), t))d\mathbf{x} = d \int_{\mathcal{V}(t)} d\mathbf{x} = \int_{\mathcal{V}(t)} \nabla \cdot \tilde{\mathbf{w}}(\mathbf{x}, t)dt d\mathbf{x} = \int_{\mathcal{V}(t_0)} (J\nabla \cdot \tilde{\mathbf{w}})(\mathbf{X}_t(\mathbf{x}), t)dt d\mathbf{x}. \quad (5)$$

Together with the incompressibility of the random term, the incompressibility condition reads thus:

$$\nabla \cdot \boldsymbol{\sigma} = 0 \text{ and } \nabla \cdot \tilde{\mathbf{w}} = 0. \quad (6)$$

In the case of an incompressible large-scale flow component, \mathbf{w} , this reduces to:

$$\nabla \cdot \boldsymbol{\sigma} = 0 \text{ and } \nabla \cdot \mathbf{w} = \nabla \cdot (\nabla \cdot \mathbf{a})^T = 0. \quad (7)$$

Note that for a divergence-free isotropic random field such as the Kraichnan model [36] the last condition is naturally satisfied, since this unresolved velocity component is associated with a constant variance tensor.

2.2. Mass conservation

Applying the RTT to the fluid density, ρ , and canceling this expression for arbitrary volumes, we get the following mass conservation constraint:

$$d_t \rho_t + \nabla \cdot (\rho \tilde{\mathbf{w}})dt + \nabla \rho \cdot \boldsymbol{\sigma} dB_t = \frac{1}{2} \nabla \cdot (\mathbf{a} \nabla q)dt, \quad (8)$$

$$\tilde{\mathbf{w}} = \mathbf{w} - \frac{1}{2} \nabla \cdot \mathbf{a}. \quad (9)$$

For an incompressible fluid with constant density, together with a volume-preserving (isochoric) condition on the large-scale velocity component, we retrieve the incompressibility conditions (7). It can be noted also that equation (8) still constitutes a transport equation since it preserves energy. As a matter of fact, it can be shown that the energy intake brought by the small-scale component is exactly compensated by the energy dissipation associated to the diffusion term [64]. This key property has been found to be essential in the modeling of physically pertinent large-scale stochastic dynamics for geophysical flows [65, 66].

2.3. Linear momentum conservation

The application of the stochastic version of the RTT to the stochastic momentum and the introduction of the forces acting on the flow enables to derive from the second Newton law the following Navier-Stokes equations [49]:

$$\left(\partial_t \mathbf{w} + \mathbf{w} \nabla^T (\mathbf{w} - \frac{1}{2} \nabla \cdot \mathbf{a}) - \frac{1}{2} \sum_{ij=1}^d \partial_{x_i} (a_{ij} \partial_{x_j} \mathbf{w})\right) \rho = \rho \mathbf{g} - \nabla p + \mu \Delta \mathbf{w}, \quad (10a)$$

$$\nabla p'_t = -\rho \mathbf{w} \nabla^T \boldsymbol{\sigma} d\mathbf{B}_t + \mu \Delta (\boldsymbol{\sigma} d\mathbf{B}_t), \quad (10b)$$

$$\nabla \cdot (\boldsymbol{\sigma} d\mathbf{B}_t) = 0, \quad \nabla \cdot \mathbf{w} = 0, \quad \nabla \cdot (\nabla \cdot \mathbf{a}) = 0. \quad (10c)$$

In this expression μ is the dynamic viscosity, $p(\mathbf{x}, t)$ denotes the large-scale (slow) pressure contribution and p'_t is a zero-mean turbulent pressure related to the small-scale velocity component. Similarly to the classical Reynolds decomposition, the dynamics of the resolved component includes an additional stress term that depends here on the resolved velocity component. A correction of the advection velocity also occurs. Both terms depend on the variance tensor which gathers the action of the turbulent fluctuations on the large-scale velocity.

It can be observed that the large-scale energy evolution is dissipative. This generalizes thus the Boussinesq 1877 assumption, which conjectures a dissipative effect of the turbulent fluctuations on the mean flow. In the case of a divergence-free isotropic random field (with a constant diagonal variance tensor), this system boils down to an intuitive constant eddy viscosity diffusivity model:

$$(\partial_t \mathbf{w} + \mathbf{w} \nabla^T \mathbf{w} - \gamma \frac{1}{2} \Delta \mathbf{w}) \rho = \rho \mathbf{g} - \nabla p + \mu \Delta \mathbf{w}, \quad \nabla \cdot \mathbf{w} = 0, \quad (11)$$

where the Laplacian dissipation term is augmented by the random field variance. The use of constant eddy viscosity thus finds here its justification as a direct consequence of an isotropic turbulence assumption.

The subgrid stress tensor involved in our formalism constitutes an anisotropic diffusion whose preferential directions of diffusion are given by the small-scale velocity variance tensor. Setting the diffusion tensor, $\boldsymbol{\sigma}$, or its associated variance tensor allows us to define directly the subgrid diffusion term and the effective advection. For instance imposing to the small-scale random velocity to live on the iso-density surfaces provides immediately a clear justification of the isopycnal diffusion employed in oceanic circulation models [49]. The specification of

the turbulent fluctuations in terms of a stochastic process provides a means to interpret different subgrid models but also to devise new ones either through *a priori* specifications or data-driven strategies.

General invariance properties of the proposed large-scale representation are listed in the appendix Appendix A. We briefly summarize them here. It is in particular shown that the distribution of the velocity anomaly is in the general case not Gaussian and does not consequently correspond to normal or quasi-normal approximations [52, 54]. We show that this stochastic representation has remarkable invariance properties; it is Galilean invariant and preserves (in the absence of molecular viscosity) the Euler equations' scale invariance properties. Otherwise, a useful scaling for the variance tensor is derived from the Kolmogorov-Richardson scaling and a dimensionless number relating the large-scale kinetic energy to a characteristic value of the velocity variance at the resolved scale.

3. Numerical simulation and assessment

In this section we assessed, through numerical simulations, the performances of the proposed large-scale dynamics for different variance tensor models. Those simple models have been defined from local statistics of the resolved component and compared to the classical Smagorinsky subgrid model associated with a dynamical procedure [22, 44]. Those numerical experiments have been performed on the Taylor-Green flow [74].

3.1. Taylor-Green vortex flow simulation

Taylor-Green vortex flow is a critical test for numerical schemes, as both the convective term and viscous term play important roles. Due to the energy cascade generated by the convective term, the flow becomes rapidly turbulent with the creation of small-scale structures up to a dissipation peak. This stage is followed by a decay phase similar to a decaying homogeneous turbulence. This flow is considered as a prototypical system to study the production of small-scale eddies due to vorticity increase and vortex stretching mechanism [7, 8, 55, 74]. As for triperiodic flows, dissipation and enstrophy are similar up to twice the viscosity coefficient, the first stage corresponds to an enstrophy production due to vortex stretching mechanism whereas the enstrophy almost constantly decays in the second phase within a turbulent cascade driven by the viscous effects. As a consequence, a precise and high-order representation of the viscous and convective terms is needed to get an accurate numerical simulation.

In Cartesian coordinates, this flow is defined by the following initial conditions:

$$\begin{aligned} u(x, y, z) &= U_0 \sin\left(\frac{x}{L_0}\right) \cos\left(\frac{y}{L_0}\right) \cos\left(\frac{z}{L_0}\right), \\ v(x, y, z) &= -U_0 \cos\left(\frac{x}{L_0}\right) \sin\left(\frac{y}{L_0}\right) \cos\left(\frac{z}{L_0}\right), \\ w(x, y, z) &= 0, \end{aligned}$$

and

$$p(x, y, z) = p_0 + \frac{\rho U_0^2}{16} \left(\cos\left(\frac{2x}{L_0}\right) + \cos\left(\frac{2y}{L_0}\right) + \cos\left(\frac{2z}{L_0}\right) + 2 \right).$$

The computation domain is defined as a cubic box with periodic boundary conditions on all the faces. The length of the domain is set to 2π in each of the axis direction, which gives a characteristic length $L_0 = 2\pi$ and a Reynolds number $Re = U_0 L_0 / \nu$. In the literature, several high-order numerical methods have been tested for the direct numerical simulation (DNS) of the Taylor-Green vortex flow, see [13, 75] and references therein. In this study we used a discrete scheme built on a divergence-free wavelet basis [32, 33]. This scheme presents several computational advantages. First of all, it guarantees a divergence-free solution in the physical domain with a good numerical complexity. Besides, as the spatial filters considered corresponds to a multi-resolution projection, two successive filtering operations can be switched together. This property reveals useful within the Germano dynamic strategy enabling to estimate the subgrid tensor weight factor. This numerical scheme achieves similar performances to a pseudo-spectral method.

3.2. Analysis criterion

The different numerical simulations performed are mainly assessed and compared according to the evolution along time of the following criterion:

- The mean kinetic energy (KE)

$$\mathcal{E}(t) = \frac{1}{2|\Omega|} \int_{\Omega} \mathbf{w} \cdot \mathbf{w} d\mathbf{x}.$$

- The mean kinetic energy dissipation rate

$$\epsilon(t) = \frac{2\nu}{|\Omega|} \int_{\Omega} \mathbf{S} : \mathbf{S} d\mathbf{x}, \quad (12)$$

where \mathbf{S} is the rate of strain tensor: $S_{ij} = \frac{1}{2} (\partial_{x_i} w_j + \partial_{x_j} w_i)$. The mean kinetic energy is linked to the dissipation rate by:

$$\epsilon(t) = -\frac{d\mathcal{E}}{dt}. \quad (13)$$

To clearly separate those two forms of the energy dissipation we will denote $\epsilon_{\mathcal{E}}(t)$ the expression computed from the kinetic energy differentiation and $\epsilon_S(t)$ the dissipation computed from the rate of strain norm. In the sequel, all those averaged quantities are computed in their dimensionless form:

$$t := \frac{tU_0}{L_0} = t_c, \quad \mathcal{E}(t) := \frac{\mathcal{E}(t)}{U_0^2} \quad \text{and} \quad \epsilon(t) := \frac{\epsilon(t)L_0}{U_0^3},$$

where t_c denotes the convective time. The temporal evolution of those mean energy quantities enable to monitor the quality of the solution over time and to assess the accuracy of the discrete scheme used for the velocity gradients. In addition to those criterion, we will plot the energy spectrum of the resolved velocity at several distinct instants.

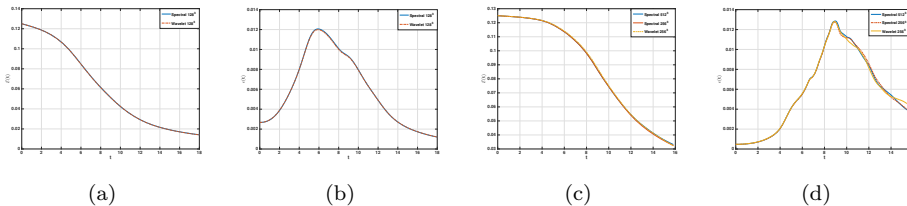


Figure 1: Comparison between the divergence-free wavelet numerical scheme and the Fourier pseudo-spectral scheme. Evolution of the dimensionless energy \mathcal{E} (a) – and (c)– and its dissipation rate ϵ_S (b) – and (d) – as a function of the dimensionless time for $Re = 280$ and $Re = 1600$ respectively.

3.3. Direct Numerical Simulation of the Taylor-Green flow

We evaluated first the ability of the divergence-free wavelet based method to reproduce faithfully the main features of the Taylor-Green flow. For this purpose, two different direct numerical simulations have been conducted.

The first experiment concerns a simulation at a low Reynolds number: $Re = 280$. For this case the divergence-free wavelet has been run on a regular grid of 128^3 points. For comparison purpose we performed a classical pseudo-spectral simulation with 128^3 Fourier modes. Let us note that at this low Reynolds number ($Re = 280$), only 64^3 Fourier modes are required to represent accurately all the hydrodynamics scales in the limit of $\delta x \leq \eta$, where η is the Kolmogorov scale [13]. The time evolution of the mean kinetic energy and the mean dissipation rate obtained for both methods are plotted on figures 1(a) and 1(b) respectively. As can be observed the solutions superimpose almost perfectly. For both methods the energy dissipation computed from the rate of strain tensor norm, ϵ_S , and from the kinetic energy differentiation, $\epsilon_{\mathcal{E}}$, fully coincide. We therefore plotted here only the rate of strain norm.

In a second experiment, both simulations have been then carried out for a moderate Reynolds number fixed at $Re = 1600$. Since the study of [7], numerous numerical experiences have been conducted to understand accurately the dynamic of the Taylor-Green vortex flow at this Reynolds number. As mentioned in [13, 75], all the scales of the flow are captured with a 512^3 mesh grid but 256^3 degrees of freedom are sufficient to represent its main characteristics. We therefore run the divergence-free wavelet based simulation at this latter resolution. We also performed a Fourier pseudo-spectral simulation with a desaliasing procedure at the same resolution. On figures 1(c) and 1(d), we displayed, for both simulations, the kinetic energy and dissipation rate time evolutions. On the same figures, for comparison purpose, we also plotted the curves corresponding to a 512^3 Fourier modes pseudo-spectral solution (with desaliasing) available from [13]. As in the previous case the dissipation ϵ_S fully matches $\epsilon_{\mathcal{E}}$ and thus only the rate of strain tensor norm is shown in figure 1(d). The divergence-free wavelet simulation is in good agreement with the spectral reference solution, especially before the dissipation peak when the convective

phenomena is predominant. Slight discrepancies appear in the decaying phase starting after the dissipation peak ($t_c \approx 8.95$).

Those experiments show that the divergence-free wavelet scheme provides results of comparable quality to those obtained from pseudo-spectral simulations at identical resolutions. In the following all the LES studied were carried out with this scheme. Let us point out we did not rely on the symmetries of the Taylor-Green flow to compute the wavelet numerical simulations, neither for the DNS nor for the LES. The performances of various subgrid modeling are discussed in section 3.5. Before that, we present in the next section the different variance tensor models that have been experimented.

3.4. Variance tensor and subgrid modelling

One of the main advantages of the stochastic formalism we propose lies in the great flexibility of the anisotropic diffusion specification. The variance tensor, \mathbf{a} , can be fixed from *a priori* shapes imposed either directly on the small scale variance or on the diffusion tensor. In some cases, such knowledge could probably be inferred from the physical approximations considered to constitute the model. Aspect ratio simplifications and/or boundary conditions that are not perfectly known could be used as well to constrain the small-scale velocities to live on specific iso-surface. Another route would consist in specifying the turbulent velocity components from small-scale measurements statistics. Despite all those directions are worth exploring as they open new strategies to design sub-grid tensors, we choose in this study to focus on several simple models.

3.4.1. Empirical specification through local mean

The first model consists in assuming an ergodic assumption to compute the variance tensor from local statistics of the resolved velocity component. The variance tensor is here defined from empirical velocity covariance computed on a local neighborhood:

$$a_{ij}(\mathbf{x}, n\delta t) := \left(\frac{L}{\eta}\right)^{5/3} \delta t \langle (w_i(\mathbf{y}, n\delta t) - \mu_i(\mathbf{x}, n\delta t))(w_j(\mathbf{y}, n\delta t) - \mu_j(\mathbf{x}, n\delta t)) \rangle_{\mathbf{y} \in \mathcal{W}(\mathbf{x}, n\delta t)},$$

where $\mu_i(\mathbf{x}, n\delta t)$ denotes the empirical mean on a spatial or temporal window $\mathcal{W}(\mathbf{x}, n\delta t)$, L is the spatial scale considered for the simulation, which corresponds to a mesh grid composed of 2^{3L} grid points, and η is the Kolmogorov scale. The empirical averaging, $\langle \cdot \rangle$, is computed either spatially over a small $(3 \times 3 \times 3)$ window centered around point \mathbf{x} or temporally, at point \mathbf{x} , over the time interval $[(n-2)\delta t, n\delta t]$. In the following, they are referred to as the spatial and temporal local covariances respectively. Both models are weighted by the variance tensor scale ratio derived in section Appendix A.1. Let us note those two models could be easily combined to define a spatio-temporal scheme.

3.4.2. Optimal specification through scale similarity

The second model is defined from two successive filtering of the resolved velocity component and a scale similarity assumption. The first filtering is here defined through the associated wavelet multi-scale projector. More precisely, since the velocity $\mathbf{w}(\mathbf{x}, t)$ can be decomposed as:

$$\mathbf{w}(\mathbf{x}, t) = \mathcal{P}_\ell[\mathbf{w}(\mathbf{x}, t)] + \sum_{|j| \geq |\ell|} \mathcal{Q}_j[\mathbf{w}(\mathbf{x}, t)], \quad \mathcal{Q}_j = \mathcal{P}_{j+1} - \mathcal{P}_j, \quad (14)$$

where \mathcal{P}_j denotes the projector onto the scaling functions basis [17, 33], the resolved filtered velocity $\mathbf{w}_\ell(\mathbf{x}, t)$ is given by:

$$\mathbf{w}_\ell(\mathbf{x}, t) := \mathcal{P}_\ell[\mathbf{w}(\mathbf{x}, t)]. \quad (15)$$

The second, so called “test”, filtering is defined by the projection of $\mathbf{w}_\ell(\mathbf{x}, t)$ onto resolution $\ell' = \ell - 1$, which is the immediate coarser resolution following the simulation scale:

$$\widetilde{\mathbf{w}}_{\ell'}(\mathbf{x}, t) := \widetilde{\mathbf{w}}_\ell(\mathbf{x}, t) = \mathcal{P}_{\ell'}[\mathbf{w}(\mathbf{x}, t)]. \quad (16)$$

The stochastic Navier-Stokes equations (10a) rewritten respectively for \mathbf{w}_ℓ and $\widetilde{\mathbf{w}}_{\ell'}$ reads:

$$\partial_t \mathbf{w}_\ell + \mathbf{w}_\ell \nabla^T \mathbf{w}_\ell - \frac{1}{2} \sum_{i,j=1}^d \partial_{x_i} \partial_{x_j} (a_{ij}^\ell \mathbf{w}_\ell) = -\frac{1}{\rho} \nabla p_\ell + \nu \Delta \mathbf{w}_\ell + \mathbf{f}_\ell, \quad (17)$$

and

$$\partial_t \widetilde{\mathbf{w}}_{\ell'} + \widetilde{\mathbf{w}}_{\ell'} \nabla^T \widetilde{\mathbf{w}}_{\ell'} - \frac{1}{2} \sum_{i,j=1}^d \partial_{x_i} \partial_{x_j} (a_{ij}^{\ell'} \widetilde{\mathbf{w}}_{\ell'}) = -\frac{1}{\rho} \nabla p_{\ell'} + \nu \Delta \widetilde{\mathbf{w}}_{\ell'} + \mathbf{f}_{\ell'}. \quad (18)$$

Taking the difference of the momentum equations (17) and (18) for the two subsequent levels ℓ and ℓ' provides the residual dynamics:

$$\begin{aligned} \partial_t \bar{\mathbf{w}}_\ell + \frac{1}{\rho} \nabla \bar{p}_\ell - \nu \Delta \bar{\mathbf{w}}_\ell - \bar{\mathbf{f}}_\ell = \\ - \left(\mathbf{w}_\ell \nabla^T \mathbf{w}_\ell - \widetilde{\mathbf{w}}_{\ell'} \nabla^T \widetilde{\mathbf{w}}_{\ell'} + \frac{1}{2} \sum_{i,j=1}^d \partial_{x_i} \partial_{x_j} (a_{ij}^\ell (\mathbf{w}_\ell - \lambda \widetilde{\mathbf{w}}_{\ell'})) \right), \end{aligned} \quad (19)$$

where $\bar{\mathbf{w}}_\ell = \mathbf{w}_\ell - \widetilde{\mathbf{w}}_{\ell'}$, $\bar{\mathbf{f}}_\ell = \mathbf{f}_\ell - \mathbf{f}_{\ell'}$, and $\lambda \in \mathbb{R}$. Note that a similarity assumption $\mathbf{a}^{\ell'} = \lambda \mathbf{a}^\ell$ has been imposed for the variance tensor. It can be noticed that, if the projector \mathcal{P}_ℓ commutes with differentiation, due to the filtering projection property, the Stokes equation in the left-hand side cancels after a test filtering (*i.e.* projecting at scale ℓ'). Then, instead of solving the right-hand expression at level ℓ' and then projecting back at a finer level the estimated variance tensor, we rather propose to solve it at scale, ℓ , in a least squares sense. Introducing

the variance tensor incompressibility constraint we seek the minimizer of the following nonlinear functional:

$$\mathcal{J}(\mathbf{a}, \lambda) = \frac{1}{2} \left\| \mathbf{w}_\ell \nabla^T (\mathbf{w}_\ell - \frac{1}{2} \nabla \cdot \mathbf{a}^\ell) - \mathbf{w}_{\ell'} \nabla^T (\mathbf{w}_{\ell'} - \frac{\lambda}{2} \nabla \cdot \mathbf{a}^\ell) - \frac{1}{2} \sum_{i,j=1}^d \partial_{x_i} [a_{ij}^\ell] \partial_{x_j} (\mathbf{w}_\ell - \lambda \mathbf{w}_{\ell'}) \right\|_{L^2(\mathbb{R}^d)}^2,$$

with the positivity constraint:

$$\sum_{i,j=1}^d a_{ij}^\ell(\mathbf{x}, t) \xi_i \xi_j > \alpha \|\xi\|^2, \quad \forall \xi \in \mathbb{R}^d, \quad \alpha > 0,$$

In practice the minimization of the objective functional has been carried out using a quasi-newton method combined with the Broyden-Fletcher-Goldfarb-Shanno (BFGS) method [53] to approximate the Hessian matrix. The variance tensor has been assumed to be diagonal at all points. In order to impose the positivity constraint, instead of computing $\mathbf{a}(\mathbf{x}, t)$ we preferred to compute its square root $\sqrt{\mathbf{a}(\mathbf{x}, t)}$. For details on the computation of the gradient of \mathcal{J} , we refer to appendix Appendix B.

3.4.3. Smagorinsky subgrid model

The third model evaluated corresponds to the classical Smagorinsky eddy viscosity formulation,

$$\nu_t = (C_s \delta \mathbf{x}_\ell)^2 |\mathbf{S}|, \quad |\mathbf{S}| = \left(2 \sum_{i,j=1}^d S_{ij}^2 \right)^{\frac{1}{2}},$$

coupled with the Germano estimation procedure [22, 44] to fix dynamically the eddy viscosity constant from a least squares estimation [44] and a filtering of the velocity field at two consecutive scales. The “test” filtering is as previously defined by the projection of $\mathbf{w}_\ell(\mathbf{x}, t)$ onto the immediate coarser resolution $\ell' = \ell - 1$. Denoting the filtering operation $\widetilde{\mathbf{w}}_\ell = \mathbf{w}_{\ell'}(\mathbf{x}, t)$, the constant $C_s(t)$ is given by:

$$C_s^2(t) = \frac{\langle \mathcal{M}_{ij} (\mathcal{L}_{ij} - \frac{1}{3} \mathcal{L}_{kk} \delta_{ij}) \rangle}{\langle \mathcal{M}_{kl} \mathcal{M}_{kl} \rangle},$$

with

$$\mathcal{L}_{ij} = \widetilde{w_i w_j} - \widetilde{w_i} \widetilde{w_j} \quad \text{and} \quad \mathcal{M}_{ij} = 2(\delta \mathbf{x}_\ell)^2 |\widetilde{\mathbf{S}}| S_{ij} - 2(\delta \mathbf{x}_{\ell'})^2 |\widetilde{\mathbf{S}}| \widetilde{S}_{ij},$$

and $\langle \cdot \rangle$ denotes a spatial averaging.

3.5. Large-scale simulation numerical results

The performances of the different sub-grid models have been compared for two different mesh grid resolutions (64^3 and 128^3) and different Reynolds number values (e.g. 1600, 3000 and 5000). The decimation factors given by the ratio of an appropriate DNS grid over the LES mesh size are listed in table 3.5).

Table 1: Decimation factor of the LES simulations defined as the ratio of the DNS/LES spatial grid resolutions

Decimation DNS/LES	128 ³	64 ³
$Re = 1600$	2 ³	4 ³
$Re = 3000$	6.75 ³	13.5 ³
$Re = 5000$	10 ³	20 ³

3.5.1. Kinetic energy evolution and dissipation rate

For those different configurations we show the time evolution of the mean kinetic energy (left panel), the mean energy dissipation rate – computed from the rate of strain norm – (central panel) and the kinetic energy derivative (right panel). Those curves, displayed figures 3-8, are plotted for the different LES solutions and a DNS of reference. Let us note as a first remark, that the wavelet scheme used is associated to a low numerical dissipation as even in the lower Reynolds number case (1600) the higher LES resolution yields numerical explosion without an additional subgrid model. This low numerical dissipation behavior will be confirmed latter on by computing the associated effective Reynolds number [4, 18, 19, 76, 78].

We observe from those figures that all the large-scale models achieved to reproduce the right amount of kinetic energy and energy dissipation rate. However, two groups of subgrid tensor can be recognized. The first one gathers the dynamic Smagorinsky tensor (**Dyn-S**) and the variance tensor defined from the spatial local velocity covariance (**Spatial**). The second group is composed of the optimal variance tensor with a scale similarity assumption (**Opt-SS**) and the variance tensor built from the velocity temporal covariance (**temporal**). The first group (with spatial model) is more dissipative than the second group of subgrid tensor. The optimal variance tensor (**Opt-SS**) and the temporal covariance are strikingly similar whereas they are based on very different modelling. The scale similarity with an optimally tuned parameter seems to fit well the subgrid tensor associated to the temporal covariance. This confirms the relevance of the variance tensor scaling since no dynamics strategy has been performed for the spatial and temporal covariance models.

The dynamic Smagorinsky subgrid tensor is in general the most dissipative scheme. The transition advection phase is launched earlier for this model than for the others. This is noticeable for all the different cases on the mean energy dissipation rate (right panels of figures 3, 4, 5, 6, 7, and 8). The dynamic Smagorinsky model provides in general the lower kinetic energy and the lower rate of strain norm. We note that the first group of subgrid tensors exhibits in a general way a too fast dissipation in the first phase of the flow ($t \in [4, 9]$), characterized by the domination of the advection mechanism. An undue smoothing of the resolved velocity gradient results from this too high dissipation rate. This is confirmed by looking at the rate of strain norm plotted in the central panel

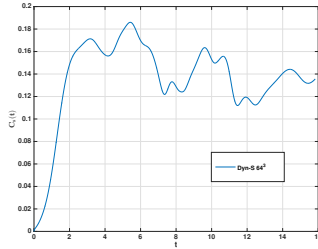


Figure 2: Time evolution of the dynamic constants of the Smagorinsky model. Taylor-Green vortex simulation at $Re = 1600$ for a 64^3 mesh grid.

of figures 3–8. This too fast dissipation is accompanied by strong variations of the dissipation rate. These variations are stronger for the dynamic Smagorinsky case. The oscillations of the Smagorinsky scheme can be observed in the advection phase, at the dissipation peak but also in the decay phase whereas the other schemes do not show such strong variations in the decay phase. Besides, strong oscillations remain around the dissipation peak when the grid mesh resolution is increased (see figures 4, 6 and 8 for $Re=1600$, $Re=3000$ and $Re=5000$ respectively) whereas for the spatial covariance model these oscillations are strongly attenuated. Let us note that, in the three cases, for the 128^3 mesh-grid the dissipation peak is slightly anticipated for the spatial covariance and the decay phase is triggered earlier than for the DNS. Nevertheless, apart from this small time shift the dissipation rate profile is regular. Within this first group, the model built from local spatial velocity covariance performs better than the original Smagorinsky tensor. For information purpose we draw on figure 2 the value along time of the dynamic Smagorinsky weighting for the 64^3 mesh grid and $Re=1600$. The obtained maximum value is about 0.1860 and the mean value is 0.1366, this is in good agreement with the predicted values, see [22]. We recall, that for the other schemes, the constant is fixed for the spatial and temporal covariance subgrid tensors (see section 3.4.1) and optimally estimated (together with the variance shape) through a similarity principle for the so-called optimal covariance scheme (section 3.4.2).

The second group of variance tensor models outperforms clearly the results of the first group. Both the temporal covariance model and the optimal variance tensor show very close results. At $Re=1600$, for a 64^3 mesh-grid the optimal variance tensor has a slightly higher dissipation rate at the dissipation peak whereas the temporal covariance model fits almost perfectly the DNS results around the dissipation peak ($t \in [8, 10]$). For a higher resolution (128^3), the optimal variance tensor matches very well the DNS dissipation curve whereas the temporal scheme provides a slight anticipation of the dissipation peak and a too slow dissipation rate in beginning of the decay phase. For higher Reynolds numbers, and low resolution grid (64^4) both schemes lead to very similar results. They show oscillations of the dissipation rate in the advection phase and in the region of the dissipation peak. For this resolution, the spatial covariance scheme

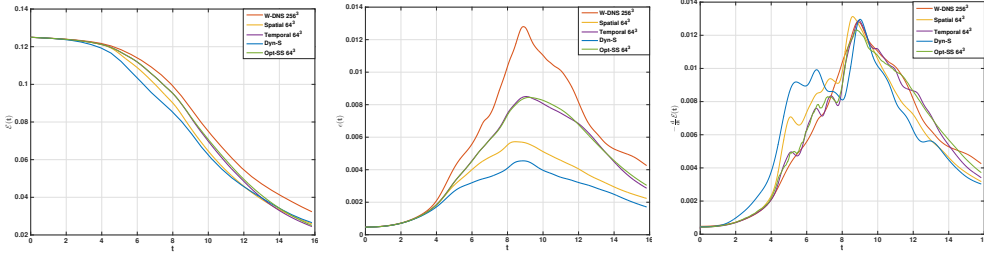


Figure 3: Evolution of the dimensionless energy $\mathcal{E}(t)$ (left) and of the energy dissipation rate $\epsilon_{\mathcal{E}} = -\frac{d}{dt}\mathcal{E}(t)$ (right) as a function of the dimensionless time. Comparison between the spatial covariance model, the dynamic Smagorinsky model and the wavelet DNS for the Taylor-Green vortex at $Re = 1600$ for a 64^3 mesh grid.

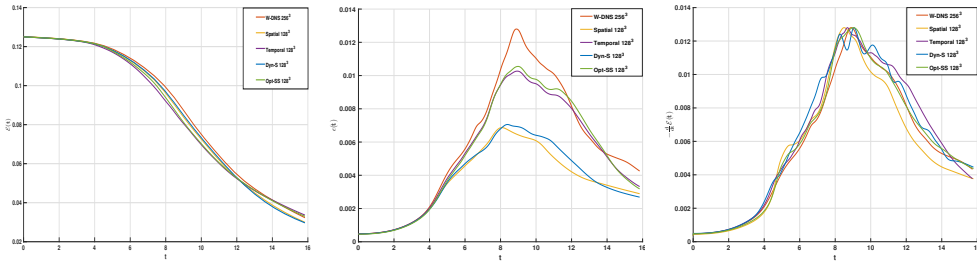


Figure 4: Evolution of the dimensionless energy $\mathcal{E}(t)$ (left) and of the energy dissipation rate $\epsilon_{\mathcal{E}} = -\frac{d}{dt}\mathcal{E}(t)$ (right) as a function of the dimensionless time. Comparison between the spatial covariance model, the dynamic Smagorinsky model and the wavelet DNS for the Taylor-Green vortex at $Re = 1600$ for a 128^3 mesh grid.

is closer to the DNS. With an augmentation of the resolution, the oscillations of the dissipation rate almost disappear for all the covariance models (opposite to the Smagorinsky model). The optimal variance tensor constructed from a similarity principle across scales and the temporal variance fits perfectly the DNS at the dissipation peak (unlike the spatial scheme which anticipates this maximum – see previous comments). The regions of maximal dissipation rate are however slightly enlarged when compared to the DNS. Both models perform similarly in the decay phase. In a general way, we note that all the models exhibit a faster decrease of the dissipation rate (or of the enstrophy) than the DNS at the beginning of the decay phase.

3.5.2. Effective Reynolds number

The effective viscosity and the resulting effective Reynolds number based on the Taylor microscale have been calculated following [78]. The mean value estimated between $t = 14$ and $t = 16$ are reported in table 3.5.2. We notice that the corresponding Reynolds number is well in the range of the targeted Reynolds number value. The optimal and temporal covariances are associated

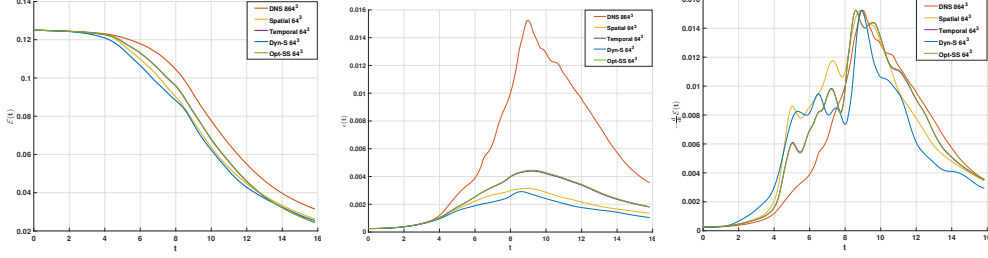


Figure 5: Evolution of the dimensionless energy $\mathcal{E}(t)$ (left) and of the energy dissipation rate $\epsilon_{\mathcal{E}} = -\frac{d}{dt}\mathcal{E}(t)$ (right) as a function of the dimensionless time. Comparison between the spatial covariance model, the dynamic Smagorinsky model and the DNS [15] for the Taylor-Green vortex at $Re = 3000$ for a 64^3 mesh grid.

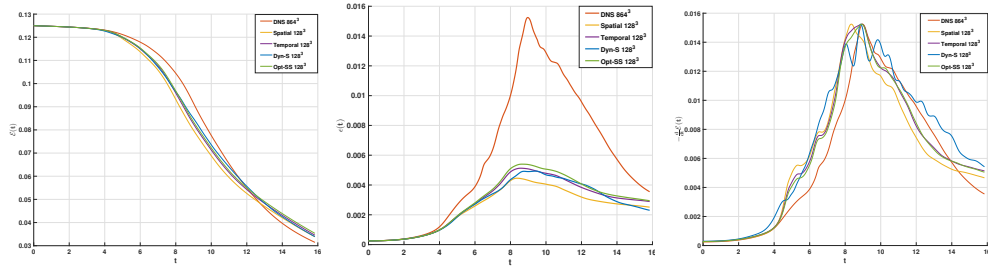


Figure 6: Evolution of the dimensionless energy $\mathcal{E}(t)$ (left) and of the energy dissipation rate $\epsilon_{\mathcal{E}} = -\frac{d}{dt}\mathcal{E}(t)$ (right) as a function of the dimensionless time. Comparison between the spatial covariance model, the dynamic Smagorinsky model and the DNS [15] for the Taylor-Green vortex at $Re = 3000$ for a 128^3 mesh grid.

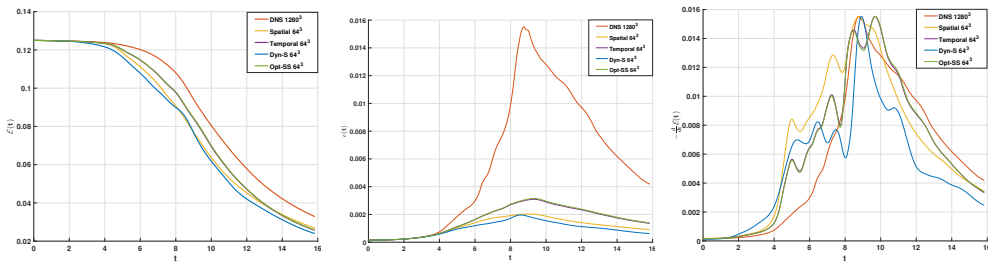


Figure 7: Evolution of the dimensionless energy $\mathcal{E}(t)$ (left) and of the energy dissipation rate $\epsilon_{\mathcal{E}} = -\frac{d}{dt}\mathcal{E}(t)$ (right) as a function of the dimensionless time. Comparison between the spatial covariance model, the dynamic Smagorinsky model and the DNS [15] for the Taylor-Green vortex at $Re = 5000$ for a 64^3 mesh grid.

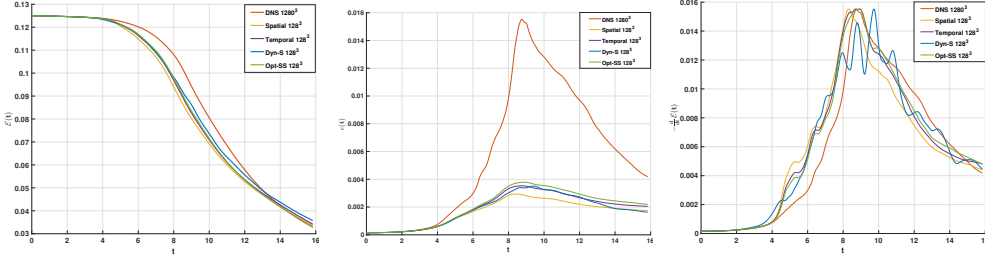


Figure 8: Evolution of the dimensionless energy $\mathcal{E}(t)$ (left) and of the energy dissipation rate $\epsilon_{\mathcal{E}} = -\frac{d}{dt}\mathcal{E}(t)$ (right) as a function of the dimensionless time. Comparison between the spatial covariance model, the dynamic Smagorinsky model and the DNS [15] for the Taylor-Green vortex at $Re = 5000$ for a 128^3 mesh grid.

to higher effective Reynolds number values than the other schemes. For a spatial resolution of 128^3 , [78] have reported significantly lower values ($Re_{\lambda} \approx [21 - 29]$) for implicit LES based on Euler equations. The values we obtained remain lower than the mixing-layer threshold ($Re_{\lambda} \approx 100$), reached by LES models only at a higher Reynolds number [15].

3.5.3. Kinetic energy spectra

We display next on figure 9 and figure 10 the energy spectrum associated to the different models for $Re=1600$. This spectrum is plotted at two different instants and two different resolutions. In addition, as we rely on a wavelet scheme for the numerical simulations, it is insightful to inspect the discrete power spectra computed from the wavelet coefficients. They are plotted on figures 11 and 12. Wavelet power spectrum corresponds to an averaged version of the Fourier spectrum [10] and exhibits the same slopes as the Fourier spectrum [58]. A discrete version of the wavelet spectrum as plotted here provides one energy measure per (wavelet) scale level.

All the models provide satisfying solutions with similar spectrum. For a 64^4 mesh grid (figure 9), the temporal and optimal variance tensor have spectrum which are in general closer to the DNS spectrum. At the end of the turbulence decay phase ($t > 13$) all the models provide close results. The dynamic Smagorinsky subgrid stress produces nevertheless a noticeable energy bump at the cutoff scale at the end of the decay phase. The energy intake of the Smagorinsky model at the cutoff scale, is clearly visible in the wavelet spectrum either at the dissipation peak or at the end of the decay phase ($t = 9$ and $t > 14$). This amplification of energy is likely due to noisy velocity fields at the cutoff. This observation is also confirmed in the study of [15] for higher Reynolds number. The three different models ensuing from our statistical representation of the small-scale velocity component does not show such a deficiency. With a finer grid (128^3) on figures 10 and 12, we see that the Smagorinsky model has an energy repartition accross scales that is significantly below the DNS. At the end of the decay phase, this energy loss, well visible in both the Fourier and wavelet

Table 2: Effective Reynolds number (mean value over the adimensional time range [14, 16]) for the different LES simulations.

	LES	Re_λ	$Re \approx Re_\lambda^2$
<hr/>			
64^3 $Re=5000$	Opt-SS	68	4600
	Temporal	68	4600
	Spatial	55	3000
	Dyn-S	60	3600
<hr/>			
128^3 $Re=5000$	Opt-SS	68	4700
	Temporal	66	4400
	Spatial	63	4000
	Dyn-S	60	3600
<hr/>			
64^3 $Re=3000$	Opt-SS	63	3900
	Temporal	63	3900
	Spatial	53	2800
	Dyn-S	56	3100
<hr/>			
128^3 $Re=3000$	Opt-SS	61	3700
	Temporal	60	3600
	Spatial	57	3200
	Dyn-S	54	2900
<hr/>			
64^3 $Re=1600$	Opt-SS	46	2100
	Temporal	46	2100
	Spatial	44	1900
	Dyn-S	38	1400
<hr/>			
128^3 $Re=1600$	Opt-SS	51	2500
	Temporal	50	2500
	Spatial	47	2200
	Dyn-S	46	2100
<hr/>			

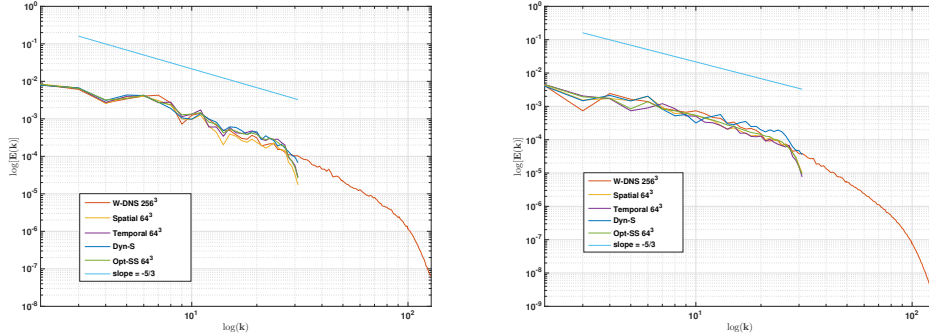


Figure 9: Total energy spectrum at $t \approx 9$ (left) and $t \approx 14.7$ (right). Comparison between the three variance tensor models, the dynamic Smagorinsky model and the DNS solution. Taylor-Green vortex at $Re = 1600$ for a 64^3 mesh grid.

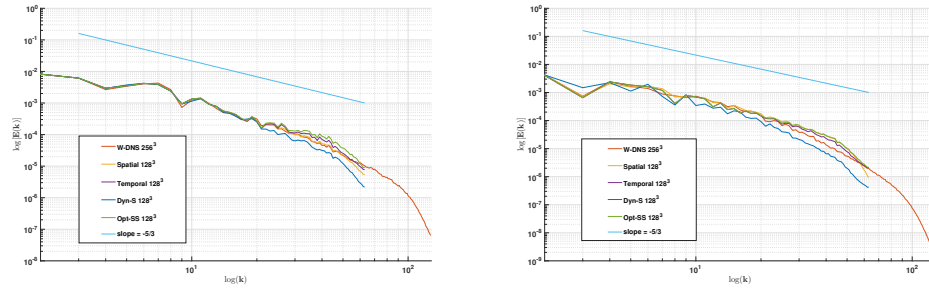


Figure 10: Total energy spectrum at $t \approx 9$ (left) and $t \approx 14.7$ (right). Comparison between the three variance tensor models, the dynamic Smagorinsky model and the DNS solution. Taylor-Green vortex at $Re = 1600$ for a 128^3 mesh grid.

spectra, concerns not only the cutoff scale, but also the intermediate scales. It affects thus relatively important structures in size (e.g. spatial scale of $1/10$). At the opposite, the solutions of the three correlation models show better energy profiles. They fit perfectly the DNS at large and intermediate scales and show an excess of energy before the cutoff, which tends to extend slightly the inertial ($-5/3$) range. In the region of the dissipation peak the spatial model fits perfectly the DNS profile. This excess of energy of the three models before the cutoff is not visible in the wavelet spectrum. On the contrary, the optimal scheme fits very well to the DNS curve, for all the wavelet scales, whereas the spatial and temporal schemes display a slight loss of energy at the smallest scales. It means that in average, across the scale, they provide solutions with the right amount of energy.

In the next figures (fig. 13 and 14) we show the Fourier and wavelet energy spectrum obtained for the different LES schemes at $Re=5000$ (for a 128^3 mesh grid). We retrieve in this case the trends observed in the previous cases.

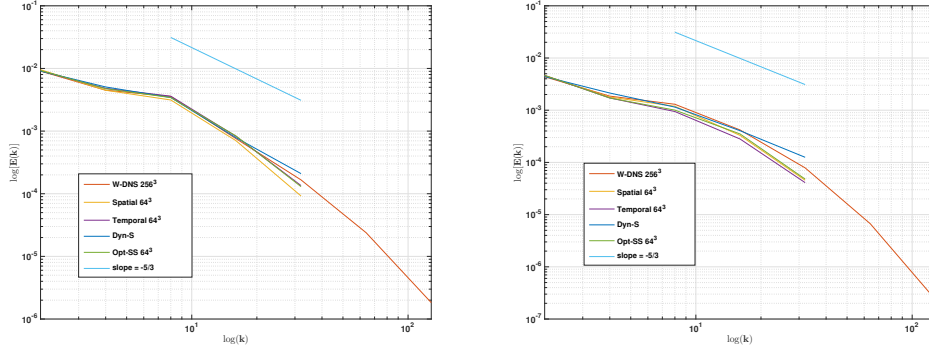


Figure 11: Wavelet energy spectrum at $t \approx 9.61$ (left) and $t \approx 14.7$ (right). Comparison between the three variance tensor models, the dynamic Smagorinsky model and the DNS solution. Taylor-Green vortex at $Re = 1600$ for a 64^3 mesh grid.

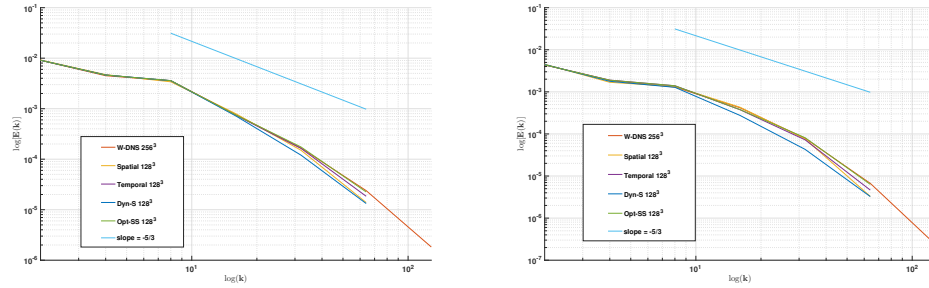


Figure 12: Wavelet energy spectrum at $t \approx 9$ (left) and $t \approx 14.7$ (right). Comparison between the three variance tensor models, the dynamic Smagorinsky model and the DNS solution. Taylor-Green vortex at $Re = 1600$ for a 128^3 mesh grid.

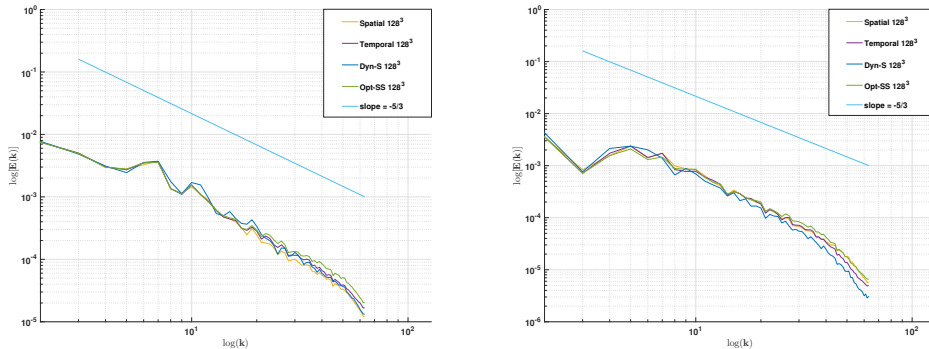


Figure 13: Total energy spectrum at $t \approx 9$ (left) and $t \approx 14.7$ (right). Comparison between the three variance tensor models, the dynamic Smagorinsky model and the DNS solution. Taylor-Green vortex at $Re = 5000$ for a 128^3 mesh grid.

For this Reynolds number, unfortunately, we do not have reference DNS data for the considered time instant. Nevertheless, the trends of the different LES schemes can be analyzed and compared. The Smagorinsky model exhibits a lower energy level than the other schemes at intermediate and small scales. As the Smagorinsky model leads to higher kinetic energy level at the end of the decay phase ($t > 14$) (left panel of figure 8), it can be inferred that the energy level reached by the Smagorinsky model at large scales corresponds clearly to an undue energy intake. In comparison, the covariance subgrid models achieved to have a kinetic energy level very close to the DNS for ($t > 14$) (left panel of figure 8). It can be also noticed that unlike the covariance schemes, the dynamic Smagorinsky model has not developed a clear turbulent $-5/3$ spectrum at the end of the decay phase. This is particularly visible in the wavelet spectrum (figure 12). This extension of the inertial range is consistent with the higher value of the effective Reynolds number observed for the covariance subgrid models – table (3.5.2). In the region of the dissipation peak, let us recall that the Smagorinsky model is subject to strong oscillations of the dissipation rate. It is therefore difficult to analyse its behavior on a single spectrum. Besides, these oscillations are likely not a good sign on the quality of the solutions provided.

Regarding the different criteria explored, there is a clear convergence of elements showing that the proposed large-scale subgrid tensors based on local velocity covariances perform better than the dynamic Smagorinsky subgrid model. Among all the models proposed, the optimal variance tensor estimation based on a two-scale similarity assumption and the variance tensor constructed from a local temporal variance of the resolved velocity field outperform significantly the others. They lead to results that are strikingly close to each other. Though very simple, the temporal covariance model weighted by a unique constant fixed through the quadratic scaling rule presented section Appendix A.1

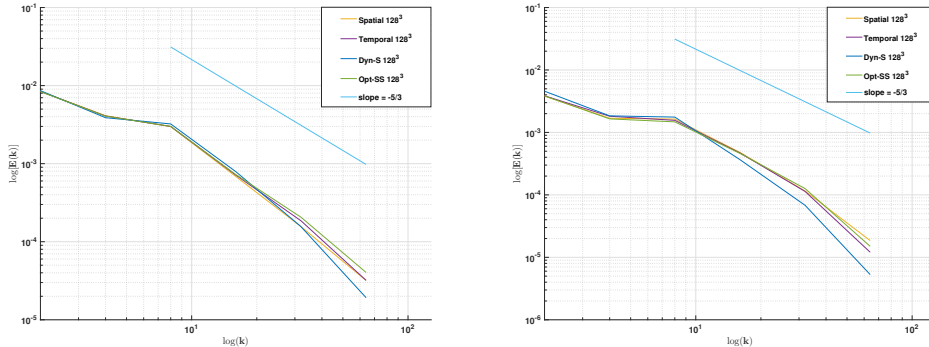


Figure 14: Wavelet energy spectrum at $t \approx 9$ (left) and $t \approx 14.7$ (right). Comparison between the three variance tensor models, the dynamic Smagorinsky model and the DNS solution. Taylor-Green vortex at $Re = 5000$ for a 128^3 mesh grid.

gives very good results. This demonstrates the pertinence of this scaling. The choices operated here are among the simplest that can be devised. More involved schemes could be easily imagined. For instance, variance tensors based on vorticity statistics might be very interesting to explore. Another route would be to elaborate this tensor from statistics extracted from measurements or DNS data. Large-eddies simulation models could likely be proposed in this spirit for non-homogeneous turbulence or boundary layer flows. Note also that both correlation schemes rely on a constant fixed through a rough dimensional scaling. A dynamical procedure in the same vein as the one used for the dynamics Smagorinsky subgrid model could be beneficial to get a finer estimate of the constant. Another interesting possibility would be to estimate this coefficient and the covariance shape from a data assimilation scheme and high-resolution measurement [27, 77]. As our purpose was here to bring a simple demonstration of the wide potentiality offered by the proposed stochastic modeling, we leave such potential improvements to future works.

4. Conclusion

In this paper we have described a decomposition of the Navier-Stokes equations in terms of a temporally smooth velocity component and a fast oscillating random field associated to the unresolved flow component. This decomposition leads to a new large-scale representation paradigm, which can be interpreted as a large eddies simulation formalized through a time-scale separation. An advection correction and a subgrid diffusion term both emerge from this formalism. They encode respectively *turbophoresis* phenomenon and anisotropic mixing effect due to turbulence. The corresponding subgrid tensor enables us generalizing the Boussinesq eddy viscosity concept on a solid theoretical ground. Such large-scale representation have been assessed on a Taylor-Green vortex flow. We compared different models of the variance tensor built from local averaging

and a scale similarity least squares estimation procedure. The different numerical simulations outperform a standard dynamic Smagorinsky model based on Boussinesq’s eddy viscosity assumption. We believe these first results are very encouraging as more advanced models could yet yield substantial improvements. As a matter of fact this formalism, built from physical conservation laws, paves the way to new possibilities to design efficient subgrid schemes. One could for instance explore models where the diffusion tensor is learned from DNS data or from small-scale observations. Another route of investigation consists in defining adapted basis for the small-scale random field from the fluctuations observed on two consecutive scales of the resolved tensor.

Acknowledgments

The authors acknowledge the support of the “Laboratoires d’Excellence” CominLabs, Lebesgue and Mer through the SEACS project.

References

- [1] A. Aspden, N. Nikiforakis, S. Dalziel, and J.B. Bell. Analysis of implicit les methods. *App. Math. Comp. Sci.*, 3(1):103–126, 2008.
- [2] J. Bardina, J.H. Ferziger, and W.C. Reynolds. Improved subgrid scale models for large eddy simulation. volume 80, page 1357.
- [3] A. Bensoussan and R. Temam. Equations stochastique du type Navier-Stokes. *J. Funct. Anal.*, 13, 1973.
- [4] S. Bidadi and S. Rani. Investigation of numerical viscosities and dissipation rates of second-order TVD-MUSCL schemes for implicit large-eddy simulation. *J. Comp. Phys.*, 281: 1003–1031, 2015.
- [5] J.P. Boris, F.F. Grinstein, E.S. Oran, and R.L. Kolbe. New insights into large-eddy simulation. *Fluid Dyn. Res.*, 10:199–228, 1992.
- [6] J. Boussinesq. Essai sur la théorie des eaux courantes. Mémoires présentés par divers savants à l’Académie des Sciences, 23 (1): 1–680, 1877.
- [7] M. Brachet, D. Meiron, S. Orszag, B. Nickel, R. Morf, and U.Frisch. Small-scale structure of the Taylor-Green vortex. *J. Fluid. Mech.*, 130(6):411–452, 1983.
- [8] M. Brachet. Direct simulation of the three-dimensional turbulence in the Taylor-Green vortex. *Fluid. Dyn. Res.*, 8:1–8, 1991.
- [9] M. Brooke, K. Kontomaris, T. Hanratty, and J. McLaughlin. Turbulent deposition and trapping of aerosols at a wall *Phys. of Fluids*, A 4, 825–834,1992.

- [10] Ch-H. Bruneau, P. Fischer, Z. Peter, and A. Yger. Comparison of numerical methods for the computation of energy spectra in 2D turbulence. Part I: Direct methods *Sampling Theory Sign. and Im. Proc.*, 1(1):0:50, 2002.
- [11] R. Buizza, M. Miller, and T.N. Palmer. Stochastic representation of model uncertainties in the ECMWF ensemble prediction system. *Q. J. R. Met. Soc.*, 125:2887–2908, 1999.
- [12] T. Chacon-Rebollo and R. Lewandowski. *Mathematical and numerical foundations of turbulence models and applications*. Springer New-York, 2014.
- [13] J.B. Chapelier, M. De La Llave Plata, F. Renac, and E. Martin. Final abstract for ONERA Taylor- Green DG participation. In *1st International Workshop on High-Order CFD Methods at the 50th AIAA Aerospace Sciences Meeting*, Nashville,TN, 2013.
- [14] M. Caporaloni, F. Tampieri, F. Trombetti, and O. Vittori. Transfer of particles in non- isotropic air turbulence. *J. Atmos. Sci.*, 32:565-568,1975.
- [15] T. Dairay, E. Lamballais, S. Laizet, and J.C. Vassilicos. Numerical dissipation vs. subgrid-scale modelling for large eddy simulation. *J. Comp. Phys.*, 337: 252–274, 2017.
- [16] J. Deardorff. A numerical study of three-dimensional turbulent channel flow at large Reynolds numbers. *J. Fluid Mech.*, 1970.
- [17] E. Deriaz and V. Perrier. Divergence-free and curl-free wavelets in 2d and 3d, application to turbulent flows. *J. of Turbulence*, 7(3):1–37, 2006.
- [18] J. A. Domaradzki, Z. Xiao, and P. K. Smolarkiewicz. Effective eddy viscosities in implicit large eddy simulations of turbulent flows *Phys. of Fluids*, 15(12):3890–3893, 2003.
- [19] D. Drikakis, C. Fureby, F. F. Grinstein and D. Youngs. Simulation of transition and turbulence decay in the Taylor-Green vortex *J. of Turbulence*, 8(20):1–12, 2007.
- [20] C. Franzke, T. O’Kane, J. Berner, P. Williams, and V. Lucarini. Stochastic climate theory and modeling. *Wiley Interdisciplinary Reviews: Climate Change*, 6(1):63–78, 2015.
- [21] P. Gent and J. McWilliams. Isopycnal mixing in ocean circulation models. *J. Phys. Oceanogr.*, 20:150–155, 1990.
- [22] M. Germano, U. Piomelli, P. Moin, and W. H. Cabot. A dynamic subgrid-scale eddy viscosity model. *Phys. of Fluids*, 3:1760–1765, 1991.
- [23] M. Germano. Turbulence : the filtering approach. *J. Fluid Mech.*, 1992.

- [24] S. Ghosal. An analysis of numerical errors in large-eddy simulations of turbulence. *J. Comp. Phys.*, 125:187–206, 1996.
- [25] S. Ghosal and P. Moin. The basic equations for the large eddy simulation of turbulent flows in complex geometry. *J. Comp. Phys.*, 1995.
- [26] F. F. Grinstein, L. G. Margolin, and W. J. Rider,. *Implicit Large Eddy Simulation: Computing Turbulent Flow Dynamics*. Cambridge University Press, 2010.
- [27] A. Gronsksis, D. Heitz, and E. Mémin. Inflow and initial conditions for direct numerical simulation based on adjoint data assimilation. *J. Comp. Phys.*, 242(6):480–497, 2013.
- [28] I. Grooms and A. Majda. Efficient stochastic superparameterization for geophysical turbulence. *PNAS*, 110(12), 2013.
- [29] D. Haworth and S. Pope. A generalized Langevin model for turbulent flows. *Phys. of Fluids*, 29:387–405, 1986.
- [30] D. Holm Variational principles for stochastic fluid dynamics. *Proc. R. Soc. A* 471(ISSN: 1364-5021), 2015.
- [31] B. Dubrulle J.-P Laval and J.C. McWilliams. Langevin models of turbulence: Renormalization group, distant interaction algorithms or rapid distortion theory? *Phys. of Fluids*, 15(5):1327–1339, 2006.
- [32] S. Kadri-Harouna, P. Dérian, P. Héas, and E. Mémin. Divergence-free wavelets and high order regularization. *International Journal of Computer Vision*, 103(1):80–99, 2013.
- [33] S. Kadri-Harouna and V. Perrier. Effective construction of divergence-free wavelets on the square. *J. Comp. and Applied Math.*, 2013.
- [34] G. Karamanos and G. Karniadakis. A spectral vanishing viscosity method for large-eddy simulations. *J. Comp. Phys.*, 163(1):22–50, 2000.
- [35] R. Kraichnan. The structure of isotropic turbulence at very high reynolds numbers. *J. Fluids Mech.*, 5:477–543, 1959.
- [36] R. Kraichnan. Small-scale structure of a scalar field convected by turbulence. *Phys. of Fluids*, 11:945–963, 1968.
- [37] R. Kraichnan. Convergents to turbulence functions. *J. Fluid Mech.*, 41:189–217, 1970.
- [38] H. Kunita. *Stochastic flows and stochastic differential equations*. Cambridge University Press, 1990.
- [39] E. Lamballais, V. Fortunè, and S. Laizet. Straightforward high-order numerical dissipation via the viscous term for direct and large eddy simulation. *J. Comp. Phys.*, 230:3270–3275, 2011.

- [40] W. Layton. Approximating the larger eddies in fluid motion v: Kinetic energy balance of scale similarity models. *Math. and Comp. Modelling*, 2000.
- [41] C. Leith. Atmospheric predictability and two-dimensional turbulence. *J. Atmos. Sci.*, 28, 1971.
- [42] C. Leith. Stochastic backscatter in a subgrid-scale model: plane shear mixing layer. *Phys. of Fluids*, 2(3):1521–1530, 1990.
- [43] D. Lilly. On the application of the eddy viscosity concept in the inertial subrange of turbulence. Tech. Report 123, NCAR, 1966.
- [44] D. Lilly. A proposed modification of the Germano subgrid-scale closure. *Phys. of Fluids*, 3:2746–2757, 1992.
- [45] J. Macinnes and F. Bracco. Stochastic particles dispersion modelling and the tracer-particle limit. *Phys. of Fluids*, 4(12):2809–2824, 1992.
- [46] A. Majda, I. Timofeyev, and E. Vanden Eijnden. Models for stochastic climate prediction. *PNAS*, 1999.
- [47] A. Majda, I. Timofeyev, and E. Vanden Eijnden. A systematic strategies for stochastic mode reduction in climate. *J. Atmos. Sci.*, 60:1705–1722, 2003.
- [48] P.J. Mason and D.J. Thomson. Stochastic backscatter in large-eddy simulations of boundary layers. *J. Fluid Mech.*, 242:51–78, 1992.
- [49] E. Mémin. Fluid flow dynamics under location uncertainty. *Geophysical & Astrophysical Fluid Dynamics*, 108(2):119–146, 2014.
- [50] C. Meneveau and J. Katz. Scale-invariance and turbulence models for large-eddy simulation. *Annu. Rev. Fluid. Mech*, 32:1–32, 2000.
- [51] J.-P. Minier S. Chibbaro and S. Pope. Guidelines for the formulation of Lagrangian stochastic models for particle simulations of single-phase and dispersed two-phase turbulent flows. *Phys. of Fluids*, 26,1113303, 2014.
- [52] A.S. Monin and A.M. Yaglom. *Statistical fluid mechanics*, volume II. MIT Press, 1975.
- [53] J. Nocedal and S.J. Wright. *Numerical optimization*. Springer Series in Operations Research. Sringer-Verlag, New-York, 1999.
- [54] S. Orszag. Analytical theories of turbulence. *J. Fluid Mech.*, 41:363–386, 1970.
- [55] S. Orszag. Numerical simulation of the taylor-green vortex. In Springer-Verlag, editor, *International Symposium on Computing Methods in Applied Sciences and Engineering*, volume 2, pages 50–64, 1974.

- [56] T. Palmer and P. Williams. Theme issue 'stochastic physics and climate modelling'. *Phil. Trans. R. Soc.*, 366(1875), 2008.
- [57] R. Pasquetti. Spectral vanishing viscosity method for large-eddy simulation of turbulent flows. *J. Sci. Comp.*, 27(1-3):365–375, 2006.
- [58] V. Perrier, T. Philipovitch, and C. Basdevant. Wavelet spectra compared to Fourier spectra *J. Math. Phys.*, 36:1506–1519, 1995.
- [59] U. Piomelli, W. Cabot, P. Moin, and S. Lee. Subgrid-scale backscatter in turbulent and transitional flows. *Phys. of Fluids*, 3(7):1766–1771, 1991.
- [60] S. Pope. Lagrangian PDF methods for turbulent flows. *Annu. Rev. Fluid Mech.*, 26:23-63, 1994.
- [61] S. Pope. *Turbulent flows*. Cambridge University Press, 2000.
- [62] L. Prandtl. Bericht uber untersuchungen zur ausgebildeten turbulenz. *Angew. Math, Meth.*, 5:136–139, 1925.
- [63] G. Da Prato and J. Zabczyk. *Stochastic equations in infinite dimensions*. Cambridge University Press, 1992.
- [64] V. Resseguier, E. Mémin, and B. Chapron. Geophysical flows under location uncertainty, Part I Random transport and general models. *Geophysical & Astrophysical Fluid Dynamics*, in press 2017.
- [65] V. Resseguier, E. Mémin, and B. Chapron. Geophysical flows under location uncertainty, Part II Quasi-geostrophy and efficient ensemble spreading. *Geophysical & Astrophysical Fluid Dynamics*, in press 2017.
- [66] V. Resseguier, E. Mémin, and B. Chapron. Geophysical flows under location uncertainty, Part III: SQG and frontal dynamics under strong turbulence conditions. *Geophysical & Astrophysical Fluid Dynamics*, in press 2017.
- [67] P. Sagaut. *Large-eddy simulation for incompressible flow - An introduction, third edition*. Springer-Verlag, Scientific Computation series, 2005.
- [68] B. Sawford. Generalized random forcing in random-walk models of turbulent dispersion models. *Phys. of Fluids.*, 29:3582–3585, 1986.
- [69] U. Schumann. Stochastic backscatter of turbulence energy and scalar variance by random subgrid-scale fluxes. *Proc. R. Soc. A*, 451:293–318, 1995.
- [70] G. Sehmel. Particle deposition from turbulent air flow. *J. Geophys. Res.*, 75:1766–1781, 1970.
- [71] G. Shutts. A kinetic energy backscatter algorithm for use in ensemble prediction systems. *Quarterly Journal of the Royal Meteorological Society*, 612:3079–3012, 2005.

- [72] J. Smagorinsky. General circulation experiments with the primitive equation: I. the basic experiment. *Monthly Weather Review*, 91:99–165, 1963.
- [73] E. Tadmor. Convergence of spectral methods for nonlinear conservation laws. *SIAM J. Numer. Anal.*, 26(1):30–44, 1989.
- [74] G. Taylor and A. Green. Mechanisms of the production of small eddies from large ones. *Proc. R. Soc. A*, 1938.
- [75] W. M. Van Rees, D. I. Leonard, A. Pullin, and P. Koumoutsakos. A comparison of vortex and pseudo-spectral methods for the simulation of periodic vortical flows at high Reynolds numbers. *J. Comp. Phys*, 230:2794–2805, 2011.
- [76] A. J. Wachtor, F. F. Grinstein, C. R. DeVore, J. R. Ristorcelli, and L. G. Margolin. Implicit large-eddy simulation of passive scalar mixing in statistically stationary isotropic turbulence. *Phys. of Fluids*, 25, 025101230, 2013.
- [77] Y. Yang, and E. Mémin. High-resolution data assimilation through stochastic subgrid tensor and parameter estimation from 4DEnVar. *Tellus A*, 69(1), 2017.
- [78] Y. Zhou, F. F. Grinstein, J. Wachtor, and B. M. Haines. Estimating the effective Reynolds number in implicit large-eddy simulation. *Phys. Rev. E*, 89, 013303, 2014.

Appendix A. General properties of the large-scale stochastic Navier-Stokes model

First of all, it is important to emphasize that the distribution of the velocity anomaly, $\mathbf{U}(\mathbf{x}, t) - \mathbb{E}\mathbf{U}(\mathbf{x}, t)$, with the Eulerian velocity field

$$\mathbf{U}(\mathbf{x}, t) = \mathbf{w}(\mathbf{x}, t) + \dot{\mathbf{W}}(\mathbf{x}, t) \quad (\text{A.1})$$

is, in the general case, *not* Gaussian. As a matter of fact, due to the multiplicative noise (the diffusion tensor depends *a priori* on the flow) and as the resolved dynamics is nonlinear, the ensemble mean of the flow velocity is in general not given by $\mathbf{w}(\mathbf{x}, t)$. Hence, this construction does not correspond to a turbulence model with a Gaussian closure hypothesis of the fourth-order correlation functions as considered in the Millionschikov hypothesis [52]. Nor is it based on quasi-normal approximations such as the EDQNM approaches [54], which opposite to the previous hypothesis ensures the positivity of the energy spectrum. In the proposed decomposition, the velocity is clearly a Markovian stochastic process, but its distribution is not Gaussian. Note also that in our approach no isotropic assumption on the increments nor on the random component are considered to define the subgrid tensor.

As already mentioned, the proposed stochastic representation can be interpreted as a temporal decomposition of the original Navier-Stokes equations. In the following sections we list several properties of this model. We begin first by a useful scaling relation of the variance tensor.

Appendix A.1. Variance tensor scaling

In the conditions of Kolmogorov-Richardson scaling, at scale ℓ , the velocity increments and the eddies turn-over time scale as $u_\ell \sim \epsilon^{1/3}\ell^{1/3}$ and $\tau_\ell \sim \epsilon^{-1/3}\ell^{2/3}$ respectively, with ϵ denoting a constant energy dissipation rate across the inertial scales range. The turn-over time ratio for two different scales in this range, $\frac{\tau_L}{\tau_\ell} \sim (\frac{L}{\ell})^{2/3}$, exhibits a direct relation between a change of time scale and a change of spacial resolution. A coarsening in time yields thus a space dilation.

Besides, at scale L , we have:

$$\mathbb{E}(u_L - \mathbb{E}u_L)^2\tau_L \sim \epsilon^{1/3}L^{4/3}.$$

At the smallest scale, this quantity corresponds to the variance tensor $a_\ell = \mathbb{E}(u_\ell - \mathbb{E}u_\ell)^2\tau_\ell$. We have thus:

$$\frac{a_\ell}{\mathbb{E}(u_L - \mathbb{E}u_L)^2\tau_L} = \left(\frac{\ell}{L}\right)^{4/3}, \quad (\text{A.2})$$

Within a given cell, V_L , at scale L , the energy of the small-scale random field is given as:

$$\mathbb{E} \sum_{\mathbf{x}_i \in V(L)} \|\boldsymbol{\sigma}_\ell(\mathbf{x}_i)d\mathbf{B}_t\|^2 = a_L\tau_\ell = \left(\frac{L}{\ell}\right)^3 a_\ell\tau_\ell, \quad (\text{A.3})$$

which from (A.2) gives us:

$$\begin{aligned} a_L &\sim \left(\frac{L}{\ell}\right)^3 \left(\frac{\ell}{L}\right)^{4/3} \mathbb{E}(u_L - \mathbb{E}u_L)^2 \tau_L, \\ &\sim \left(\frac{L}{\ell}\right)^{5/3} \mathbb{E}(u_L - \mathbb{E}u_L)^2 \tau_L. \end{aligned} \quad (\text{A.4})$$

This relation provides us an expression of the scaling between the subgrid variance tensor at scale L and the resolved velocity anomalies. It will serve us to impose a proper tuning of the subgrid term when the variance tensor is defined from the resolved velocity.

Appendix A.2. Adimensionalization of large-scale stochastic Navier-Stokes equations

Considering the scaled coordinates $\mathbf{x}^* = L\mathbf{x}$, $t^* = Tt$, with velocity $\mathbf{w}^* = U\mathbf{w}$, pressure $p^* = U^2 p$ and a variance tensor $\mathbf{a}^* = A(L) \mathbf{a}$, we have:

$$\partial_{t^*} \mathbf{w}^* + \mathbf{w}^* \nabla^* (\mathbf{w}^* - \frac{1}{2} \nabla^* \cdot \mathbf{a}^*) = -\nabla^* p^* + \frac{1}{2} \sum_{i,j=1}^d \partial_{x_i^*} (a_{ij}^* \partial_{x_j^*} \mathbf{w}^*) + \nu \Delta^* \mathbf{w}^*,$$

$$\begin{aligned} \frac{U^2}{L} \partial_t \mathbf{w} + \frac{U^2}{L} \mathbf{w} \nabla^T \mathbf{w} - \frac{1}{2} \frac{UA(L)}{L^2} \mathbf{w} \nabla^T \nabla \cdot \mathbf{a} = \\ - \frac{U^2}{L} \nabla p + \frac{1}{2} \frac{UA(L)}{L^2} \sum_{i,j=1}^d \partial_{x_i} (a_{ij} \partial_{x_j} \mathbf{w}) + \frac{U}{L^2} \nu \Delta \mathbf{w}. \end{aligned}$$

Assuming, as in the previous section, that the characteristic value of the resolved variance tensor, $A(L)$, depends linearly on the variance tensor at the smallest scale, $A(\ell)$, the dimensionless form of the large-scale stochastic Navier-Stokes equations reads:

$$\partial_t \mathbf{w} + \mathbf{w} \nabla^T (\mathbf{w} - \frac{1}{\Upsilon} \nabla \cdot \mathbf{a}) = -\nabla p + \frac{1}{\Upsilon} \sum_{i,j=1}^d \partial_{x_i} (a_{ij} \partial_{x_j} \mathbf{w}) + \frac{1}{Re} \Delta \mathbf{w}, \quad (\text{A.5})$$

where we introduced a dimensionless number

$$\Upsilon = \frac{2U^2}{K(L/\ell) \Sigma_U}, \quad (\text{A.6})$$

which relates the typical kinetic energy at scale L to a characteristic value of the velocity variance, Σ_U , at the same level. In this expression we considered from (A.4) a characteristic value of the resolved variance tensor

$$A(L) = K \left(\frac{L}{\ell}\right) \Sigma_U \frac{L}{U}, \quad (\text{A.7})$$

where we introduced a scale factor ratio, $K(\frac{L}{\ell})$ (with $K(1)=1$). As previously inferred, under the Kolmogorov scaling hypothesis this ratio scales as $(L/\ell)^{5/3}$. Let us finally observe that for a typical variance tensor, $A(\ell)$, tending to zero, (A.5) tends to the original Navier-Stokes equations. It is the situation occurring when the variance tensor is negligible in front of the drift energy.

In the next section we will see that the large-scale model proposed conserves the invariance properties of the original Navier-Stokes equations.

Appendix A.3. Invariance of large-scale stochastic Navier-Stokes equations

Let us consider in the following the classical symmetry groups of the incompressible Navier-Stokes equations in a periodic domain and in the absence of external forcing.

Appendix A.3.1. Translation-invariance

Space translation invariance is achieved if the whole velocity field $\mathbf{U}^*(\mathbf{x}, t) = \mathbf{U}(\mathbf{x} - \mathbf{b}, t)$ is still a solution of the Navier-Stokes equations. In our setting we have

$$\mathbf{w}^*(\mathbf{x}, t)dt + \boldsymbol{\sigma}^*(\mathbf{x}, t)d\mathbf{B}_t = \mathbf{w}(\mathbf{x} - \mathbf{b}, t)dt + \boldsymbol{\sigma}(\mathbf{x} - \mathbf{b}, t)d\mathbf{B}_t.$$

Separating the Brownian component from the smooth term yields: $\mathbf{w}^*(\mathbf{x}, t) = \mathbf{w}(\mathbf{x} - \mathbf{b}, t)$, $\boldsymbol{\sigma}^*(\mathbf{x}, t) = \boldsymbol{\sigma}(\mathbf{x} - \mathbf{b}, t)$ and hence $\partial_t \mathbf{w}^* = \partial_t \mathbf{w}$, $\partial_{x_i} \mathbf{w}^* = \partial_{x_i} \mathbf{w}$, $\partial_{x_i} \boldsymbol{\sigma}^* = \partial_{x_i} \boldsymbol{\sigma}$, $\partial_{x_i} \mathbf{a}^* = \partial_{x_i} \mathbf{a}$, $\partial_{x_i} (a_{ij}^* \partial_{x_j} \mathbf{w}^*) = \partial_{x_i} (a_{ij} \partial_{x_j} \mathbf{w})$, and translational invariance follows immediately.

Appendix A.3.2. Time-shift invariance

Time-shift invariance is obtained recalling that Brownian motion has itself a time-shift invariance property. This property allows us to write (in law) for $t^* = t - b$:

$$\boldsymbol{\sigma}^*(\mathbf{x}, t)d\mathbf{B}_{t^*} \stackrel{L}{=} \boldsymbol{\sigma}^*(\mathbf{x}, t)d\mathbf{B}_t \triangleq \boldsymbol{\sigma}(\mathbf{x}, t - b)d\mathbf{B}_t,$$

which leads straightforwardly to time-shift invariance.

Appendix A.4. Rotational and reflectional invariance

These two symmetry groups correspond to a constant rotation or to a reflection of the coordinates system. The transformed coordinates are $x_i^* = \sum_j R_{ij} x_j$ and $U_i^* = \sum_j R_{ji} U_j(\mathbf{x}^*)$. Note that $\boldsymbol{\sigma}^* d\mathbf{B}_t = \mathbf{R}^T \boldsymbol{\sigma}(\mathbf{x}^*) d\mathbf{B}_t$, which yields $\mathbf{a}^*(\mathbf{x}) = \mathbf{R}^T \boldsymbol{\sigma}(\mathbf{x}^*) \boldsymbol{\sigma}(\mathbf{x}^*)^T \mathbf{R} = \mathbf{R}^T \mathbf{a}(\mathbf{x}^*) \mathbf{R}$ and hence $\sum_{i,j=1}^d \partial_{x_i} (a_{ij}^* \partial_{x_j} \mathbf{w}^*) = \mathbf{R}^T \sum_{i,j=1}^d \partial_{x_i} (a_{ij}(\mathbf{x}^*) \partial_{x_j} \mathbf{w}(\mathbf{x}^*))$. The invariance of the transformed Navier-Stokes equations follows immediately:

$$\begin{aligned} \mathbf{R}^T \partial_t \mathbf{w}(\mathbf{x}^*) + \mathbf{R}^T \mathbf{w}(\mathbf{x}^*) \nabla^T (\mathbf{w}(\mathbf{x}^*) - \frac{1}{2} \nabla \cdot \mathbf{a}(\mathbf{x}^*)) = \\ \mathbf{R}^T \sum_{i,j=1}^d \partial_{x_i} (a_{ij}(\mathbf{x}^*) \partial_{x_j} \mathbf{w}(\mathbf{x}^*)) - \mathbf{R}^T \nabla p(\mathbf{x}^*) + \nu \mathbf{R}^T \Delta \mathbf{w}(\mathbf{x}^*). \end{aligned} \quad (\text{A.8})$$

Appendix A.4.1. Galilean transformations invariance

A model is said to be Galilean invariant if it is invariant with respect to an inertial transformation of the representation frames: $\mathbf{x}^* = \mathbf{x} - \mathbf{V}t$, $t^* = t$. The velocity in this translated non-accelerating system of reference reads

$$\mathbf{w}^* dt + \boldsymbol{\sigma}^*(\mathbf{x}, t) d\mathbf{B}_t = \mathbf{w}(\mathbf{x} - \mathbf{V}t, t) dt + \mathbf{V} dt + \boldsymbol{\sigma}(\mathbf{x} - \mathbf{V}t, t) d\mathbf{B}_t,$$

with

$$\mathbf{a}^*(\mathbf{x}, t) = \boldsymbol{\sigma}(\mathbf{x}^*, t) \boldsymbol{\sigma}(\mathbf{x}^*, t) = \mathbf{a}(\mathbf{x}^*, t).$$

From those equations we obtain:

$$\partial_{x_j} w_i^* = \partial_{x_j} w_i, \quad (\text{A.9})$$

$$\partial_t w^* = \partial_t w - \partial_{x_j} w^i V^j, \quad (\text{A.10})$$

$$\partial_{x_i} (a_{ij}^* \partial_{x_j} \mathbf{w}^*) = \partial_{x_i} (a_{ij} \partial_{x_j} \mathbf{w}). \quad (\text{A.11})$$

As the pressure and viscous force are Galilean invariant and since $\frac{d}{dt} \mathbf{w}^* = \frac{d}{dt} \mathbf{w}$, this shows the system is Galilean invariant.

Appendix A.4.2. Time reversal invariance

As with the original Navier-Stokes equation, the stochastic model is not invariant to a time reversal transformation: $\mathbf{w}^*(\mathbf{x}, t) = -\mathbf{w}(\mathbf{x}, -t)$. This property is respected only for the Euler equation. Despite the time reversibility property of Brownian motion this loss of symmetry is due to the even nature of the quadratic tensor.

Appendix A.4.3. Scale invariance

Considering the scaled transformation:

$$\mathbf{w}^*(\mathbf{x}, t) dt + \boldsymbol{\sigma}^*(\mathbf{x}, t) d\mathbf{B}_{t^*} = \lambda^h \mathbf{w}(\lambda^{-1} \mathbf{x}, \lambda^{h-1} t) dt + \lambda^h \boldsymbol{\sigma}(\lambda^{-1} \mathbf{x}, \lambda^{h-1} t) d\mathbf{B}_{t^*},$$

we get:

$$\partial_t \mathbf{w}^* = \lambda^{2h-1} \partial_t \mathbf{w}, \quad (\text{A.12})$$

$$\partial_{x_j} w_i^* w_j^* = \lambda^{2h-1} \partial_{x_j} w_i w_j, \quad (\text{A.13})$$

$$\nabla p^* = \lambda^{2h-1} \nabla p, \quad (\text{A.14})$$

$$\boldsymbol{\sigma}^*(\mathbf{x}, t) d\mathbf{B}_{t^*} = \lambda^{\frac{1}{2}(1-h)} \boldsymbol{\sigma}(\mathbf{x}, t) d\mathbf{B}_t = \lambda^{\frac{1}{2}(h+1)} \boldsymbol{\sigma}(\mathbf{x}^*, t^*) d\mathbf{B}_t, \quad (\text{A.15})$$

$$\mathbf{a}^* = \lambda^{h+1} \mathbf{a}(\lambda^{-1} \mathbf{x}, \lambda^{h-1} t), \quad (\text{A.16})$$

$$\partial_{x_j} w_i^* \partial_{x_k} \mathbf{a}_{kj}^* = \lambda^{2h-1} \partial_{x_j} w_i \partial_{x_k} \mathbf{a}_{kj}, \quad (\text{A.17})$$

$$\partial_{x_i} (a_{ij}^* \partial_{x_j} \mathbf{w}^*) = \lambda^{2h-1} \partial_{x_i} (a_{ij} \partial_{x_j} \mathbf{w}), \quad (\text{A.18})$$

$$\Delta \mathbf{w}^* = \lambda^{h-2} \Delta \mathbf{w}. \quad (\text{A.19})$$

The two last relations highlight a very interesting property of the modified Navier-Stokes equations. When the viscosity can be neglected in comparison to

the variance tensor, the large-scale stochastic Navier-Stokes equations become scale-invariant for any values of the scale exponent. They share this property with the Euler equations. When the friction term is considered the equations are invariant only for $h = -1$.

To sum up, the large-scale stochastic representation of the Navier-Stokes equations have the remarkable feature of keeping all the symmetries of the original equations and to follow the same scale invariance property as the Euler equation when neglecting the friction term. This last property, which inherits from the time scale invariance of Brownian motion, is often not verified for large-scale eddy viscosity representations of the Euler equations.

Appendix B. Gradient of the functional \mathcal{J}

Using the condition $\nabla \cdot (\nabla \cdot \mathbf{a}) = 0$, we can write:

$$\mathcal{J}(\mathbf{a}) = \frac{1}{2} \|\bar{\mathbf{w}}_\ell \nabla^T \mathbf{w}_\ell + \mathbf{w}_{\ell'} \nabla^T \bar{\mathbf{w}}_\ell - \frac{1}{2} \sum_{i,j=1}^d \partial_{x_i} \partial_{x_j} (a_{ij}(\mathbf{w}_\ell - \lambda \mathbf{w}_{\ell'}))\|_{L^2(\mathbb{R}^d)}^2,$$

where $\bar{\mathbf{w}}_\ell = \mathbf{w}_\ell - \mathbf{w}_{\ell'}$ is the multi-scale residual term. Then, it is easy to see that:

$$\begin{aligned} & \frac{1}{\epsilon} [\mathcal{J}(\mathbf{a} + \epsilon a_{mn} \mathbb{I}) - \mathcal{J}(\mathbf{a})] \xrightarrow{\epsilon \rightarrow 0} \\ & -\frac{1}{2} \langle \partial_{x_m} \partial_{x_n} [a_{mn}(\mathbf{w}_\ell - \lambda \mathbf{w}_{\ell'})], \bar{\mathbf{w}}_\ell \nabla^T \mathbf{w}_\ell + \mathbf{w}_{\ell'} \nabla^T \bar{\mathbf{w}}_\ell - \frac{1}{2} \sum_{i,j=1}^d \partial_{x_i} \partial_{x_j} [a_{ij}(\mathbf{w}_\ell - \lambda \mathbf{w}_{\ell'})] \rangle, \end{aligned}$$

and integration by part gives:

$$\begin{aligned} & \partial_{a_{mn}} \mathcal{J}(\mathbf{a}) = \\ & -\frac{1}{2} (\mathbf{w}_\ell - \lambda \mathbf{w}_{\ell'}) \partial_{x_m} \partial_{x_n} \left(\bar{\mathbf{w}}_\ell \nabla^T \mathbf{w}_\ell + \mathbf{w}_{\ell'} \nabla^T \bar{\mathbf{w}}_\ell - \frac{1}{2} \sum_{i,j=1}^d \partial_{x_i} \partial_{x_j} [a_{ij}(\mathbf{w}_\ell - \lambda \mathbf{w}_{\ell'})] \right). \end{aligned}$$

Similarly, the derivative $\partial_\lambda \mathcal{J}$ with respect to the constant λ is given by:

$$\begin{aligned} & \partial_\lambda \mathcal{J}(\mathbf{a}) = \\ & \frac{1}{2} \sum_{m,n=1}^d a_{mn} \mathbf{w}_{\ell'} \cdot \partial_{x_m} \partial_{x_n} \left(\bar{\mathbf{w}}_\ell \nabla^T \mathbf{w}_\ell + \mathbf{w}_{\ell'} \nabla^T \bar{\mathbf{w}}_\ell - \frac{1}{2} \sum_{i,j=1}^d \partial_{x_i} \partial_{x_j} [a_{ij}(\mathbf{w}_\ell - \lambda \mathbf{w}_{\ell'})] \right). \end{aligned}$$